Nano Research 2016, 9(6): 1763–1774
DOI 10.1007/s12274-016-1069-y
Research Article
ISSN 1998-0124
CN 11-5974/O4

Noble metal nanoclusters and their *in situ* calcination to nanocrystals: Precise control of their size and interface with TiO_2 nanosheets and their versatile catalysis applications

Anwer Shoaib, Muwei Ji, Hongmei Qian, Jiajia Liu, Meng Xu, and Jiatao Zhang (✉)

Beijing Key Laboratory of Construction-Tailorable Advanced Functional Materials and Green Applications, School of Materials Science & Engineering, Beijing Institute of Technology, Beijing 100081, China

Received: 12 January 2016
Revised: 7 March 2016
Accepted: 8 March 2016

KEYWORDS
noble metal nanocluster,
organic synthesis catalyst,
cocatayst,
photocatalyst hydrogen production,
photocurrent response

ABSTRACT

In this work, we present a new versatile strategy to prepare noble metal (Au, Ag and Cu) nanoclusters on TiO_2 nanosheets in large scales with exposed (001) facets with controlled size, crystalline interface, and loading amount. By precise *in situ* calcination, the metal (M = Au, Ag, and Cu) nanocrystals with controllable size and better crystalline interface with the TiO_2 support have been prepared. The potential application of the as-prepared Au, Ag, and Cu nanoclusters on TiO_2 nanosheets as potential heterogeneous catalysts for organic synthesis, such as catalytic reduction of 4-nitrophenol to 4-aminophenol, has been demonstrated. After calcination, Au, Ag, and Cu nanocrystals were found to be proficient cocatalysts for photocatalytic H_2 evolution, particularly the Au cocatalyst. Based on precise high-resolution transmission electron microscopy (HRTEM) and inductively coupled plasma optical emission spectrometry (ICP-OES) analyses, the flexible control of their size and loading amount as well as their intimate contact with the TiO_2 nanosheet enhanced the photocatalytic H_2 evolution activity and the sensitivity of the photocurrent response of the film. Furthermore, this aqueous-directed synthesis of metal nanoclusters on a support will generate further interest in the field of nanocatalysis.

1 Introduction

Since Goodman et al. reported the sensitive size effects of titania-supported Au on its CO oxidation activity [1], noble metals (Au, Ag, and Cu)-based hybrid nanostructures have been widely researched due to their special electronic structures [$nd^{10}(n+1)s^1$] and their diverse catalysis applications, such as in heterogeneous catalysis and photocatalysis [2–5]. As reported by Bell et al., the performance of these catalysts is sensitive

Address correspondence to zhangjt@bit.edu.cn

to particle size, as their surface structures and electronic properties vary greatly in the size range of roughly 1–50 nm [6]. In addition to many profound studies on the catalysis of CO oxidation to CO_2, the application of Au nanoclusters on TiO_2 supports in the catalytic synthesis of organic molecules has also been investigated [7–9]. Furthermore, because of the nanosize-enabled sensitive electronic and optical properties of Au nanocrystals, size-controlled Au nanocrystals grown on TiO_2 supports have been used as a cocatalyst to achieve efficient photoinduced electron/hole separation and electron collection in photocatalysis [10–12]. Moreover, many investigations have indicated that the synergistic effects of the regulation of the metal nanoparticle (NP) size, the surface hetero-interaction, and the active crystal face exposure of the metal oxide support are necessary to maximize the catalyst performance [13–14].

The conversion of solar energy to hydrogen energy using an efficient photocatalytic material is considered the most worthwhile and environmentally friendly process [15–19]. TiO_2-based photocatalysis technology has attracted much attention for the effective utilization of solar energy in environmental decontamination and water-splitting for hydrogen generation since Fujishima and Honda discovered the photocatalytic splitting of water on TiO_2 electrodes in 1972 [20]. Recently, high-purity anatase TiO_2 single crystals and nanosheets with a high percentage of reactive {001} facets have been reported by Yang, Xie et al., with auspicious applications in photocatalysis [21–24]. However, the quantum efficiency of TiO_2 for water-splitting is limited due to the rapid recombination of the photogenerated electron–hole pairs [25]. To "carry" the electrons out to the surface, the noble metal nanocrystals (NCs) on TiO_2 nanostructure supports with appropriate size and hetero-interaction can serve as efficient cocatalysts for the photocatalysis reaction sites and catalyze the reactions to promote charge separation and transport driven by the junctions/interfaces formed between the cocatalyst and the light-harvesting semiconductor [26–28]. As a consequence, metal/TiO_2 composite systems, such as those in which Pt, Au, Ag, or Cu is the metal, have been applied to enhance the photocatalytic activity [29–31]. However, to achieve appropriate electronic properties on nanocluster surface and efficient electron traps and proton reduction sites on cocatalysts for either noble metal nanoclusters or nanocrystal cocatalysts, the following are necessary: (1) controllable metal/TiO_2 hybrid nanostructures with tunable metal particle size, (2) strong crystalline contact to provide an intimate interface, and (3) well-defined TiO_2 nanocrystals with active crystal face exposure [32–35]. Due to the potential applications of noble metal nanostructures with sizes ranging from cluster to nanocrystal, it is crucial to develop large-scale facile syntheses that can be used in diverse catalysis applications. Herein, we choose TiO_2 nanosheets with high exposure of active (001) facets as a support to develop a facile and versatile strategy for preparing aqueous-phase noble metal (Au, Ag, Cu)/TiO_2 hybrid nanostructures with tunable metal particle size (from nanoclusters to nanocrystals). Via programmable calcination, metal/TiO_2 hetero-nanosheets with stronger crystalline contact are obtained. The heterocatalysis of 4-nitrophenol reduction and photocatalytic H_2 evolution are then used to demonstrate the improved catalytic performance of these materials.

2 Experimental

2.1 Chemicals and materials

Analytical-grade commercially available reagents were used without further purification. Tetrabutyl titanate ($[CH_3(CH_2)_3O]_4Ti$, 98%), hydrofluoric acid (HF, 47%), hydrogen tetrachloroaurate (III) ($HAuCl_4{\cdot}4H_2O$, 99.99%), silver nitrate ($AgNO_3$), copper chloride ($CuCl_2{\cdot}2H_2O$, 99.0%), urea (H_2NCONH_2, 99%), p-nitrophenol ($C_6H_5NO_3$), ammonium formate (CH_5NO_2), ethylene glycol, and ethyl acetate were procured from Aladdin. Indium tin oxide conductive glass (ITO glass, <10 $\Omega{\cdot}sq.^{-1}$), used as a working electrode, was obtained from Zhuhai Kaivo Electronic Components Co., Ltd. (China).

2.2 Preparation of TiO_2 nanosheets with exposed (001) facets

Anatase TiO_2 nanosheets were prepared by the hydrothermal method reported by Han et al. [21]. In a typical synthesis, 10 mL of tetrabutyl titanate and 1.2 mL of hydrofluoric acid solution were mixed in a dried 50-mL Teflon autoclave under ambient conditions,

followed by hydrothermal treatment of the solution at 180 ℃ for 24 h. After being cooled to room temperature, the white precipitate was collected by centrifugation, washed with ethanol and distilled water, and then dried at 80 ℃ in an oven for 12 h.

2.3 Aqueous-phase metal nanoclusters/TiO_2 nanosheet synthesis

Metal nanoclusters/TiO_2 nanosheets were prepared by a facile liquid-phase method with slight modification using urea as a basification agent [36]. In a typical synthesis, the as-synthesized anatase TiO_2 nanosheets (200 mg) were dispersed in DI water (20 mL) under 30 min of ultrasonication followed by 15 min of vigorous stirring. Next, $HAuCl_4{\cdot}4H_2O$ (4.2×10^{-3} M), $AgNO_3$ (7.4×10^{-3} M), or $CuCl_2{\cdot}2H_2O$ (1.26×10^{-3} M) was introduced into this suspension, resulting in the deposition of approximately 1 wt.%–8 wt.% Au, Ag, or Cu metal NPs on the TiO_2 nanosheets. Urea was added with the concentration 100 times higher than that of metal sources to reduce metal ions. The suspension thermostatically heated at 90 ℃ under vigorous stirring for 2 h. The obtained precipitate was separated from the precursor solution by centrifugation (9,000 rpm for 10 min) and washed three times to remove residual ions.

2.4 Preparation of metal NPs/TiO_2 nanosheets from metal nanoclusters/TiO_2 nanosheets

The samples were dried in vacuum at 100 ℃ for 6 h, followed by calcination from room temperature to 300 ℃ at a heating rate of 2 ℃·min^{-1} for 4 h under an Ar atmosphere under a 30 mL·min^{-1} flow rate. Finally, Au/TiO_2, Ag/TiO_2, and Cu/TiO_2 photocatalysts were obtained, being dark purple, reddish brown, and light grey in color, respectively.

2.5 Catalyst characterization

The compositions and phases of the obtained photocatalysts were analyzed using a Bruker D8 Advance X–ray diffractometer with standard Cu Kα radiation (λ = 1.5406 Å). The detailed morphology and interfacial lattices were imaged by low-resolution transmission electron microscopy (TEM; JEOL JEM 1200EX working at 100 kV) and high-resolution TEM (HRTEM; FEI Tecnai G2 F20 S-Twin working at 200 kV). The exact noble metal loading of the as-prepared M/TiO_2 catalysts was determined by inductively coupled plasma optical emission spectrometry (ICP-OES; iCAP6300 IRIS Intrepid II XSP Thermo Fisher Co.) using the following measurement parameters: plasma power of 1,150 W and plasma, auxiliary, and cooling gas flow rates of 0.82, 0.7, and 14 L·min^{-1}, respectively.

2.6 Experimental setup for the catalytic reduction of 4-nitrophenol

For each reaction, a mixture of p-nitrophenol (1 mmol), the as-prepared M/TiO_2 nanocluster catalyst (40 mg) in ethylene glycol (20 mL), and ammonium formate (630 mg) was heated at 120 ℃ under stirring for 8 h under a nitrogen atmosphere. The products were placed into 3-mL vials, and the catalyst was separated by centrifugation at 12,000 rpm. The products were identified using gas chromatography (GC)-mass spectroscopy (MS), and product analysis was conducted by GC.

2.7 Photocatalytic water-splitting hydrogen production test

The photocatalytic activities for water-splitting hydrogen evolution under solar light irradiation were conducted using a commercially available measurement system (Beijing Aulight Technology Co. Ltd., China) consisting of a closed gas circulation system equipped with a top-irradiation Pyrex glass reactor. First, 30 mg of the as-prepared catalyst was suspended in 80 mL of water containing ethanol (10% of the total volume) as a sacrificial agent using magnetic stirring in a Pyrex reaction vessel. The chamber was sealed and degassed for 30 min. Next, under irradiation by a 300-W xenon lamp, the suspension was continuously stirred and maintained at room temperature during the photocatalytic reaction by a flow of cooling water. The evolved gas was quantified by GC (Jing Ke Ruida; GCSP7800, MS-5 A column, TCD, N_2 carrier). A spectroradiometer (LPE; Beijing Wuke Photoelectric Technology Co. Ltd., China) was used to calculate the total power of the incident solar light. The calculated number of incident photons was 6.75×10^{22} (see S1 in the Electronic Supplementary Material (ESM) for

detailed calculation). We note that a proper comparison between photocatalytic materials should ideally be done on the basis of apparent quantum yield [37]. Hence, the apparent quantum efficiency (QE) was measured under the same photocatalytic reaction conditions according to Eq. (1) [38, 39].

$$\text{QE}\ (\%) = \frac{\text{Number of evolved } H_2 \text{ molecules} \times 2}{\text{Number of incident photons}} \times 100 \quad (1)$$

2.8 Photocurrent response measurements

A homemade conventional three-electrode electrochemical cell with platinum wire as the counter electrode and a saturated calomel electrode (SCE) as the reference electrode were used to evaluate the photocurrent response with and without solar light irradiation. The working electrodes were prepared by spreading aqueous slurries of Au/TiO_2, Ag/TiO_2, Cu/TiO_2, and TiO_2 nanosheets over ITO glass substrates. The electrodes were then slowly dried on a warm plate. The electrolyte used in the cells was 0.2 M Na_2SO_4 aqueous solution. A 300-W Xe lamp was used as the light source. The photocurrent signal was recorded with a CHI660E electrochemistry potentiostat (Shanghai Chenhua Limited, China) connected to a personal computer. All electrochemical experiments were conducted at room temperature.

3 Results and discussion

Gram-scale anatase TiO_2 nanosheets with rectangular morphology and a uniform length and thickness of ~40 nm and 6 nm, respectively, (see TEM and SEM images in Figs. S1 and S2 in the ESM) were successfully prepared by a solvothermal method. Using anatase TiO_2 nanosheets with exposed active (001) facets, we developed a versatile strategy to deposit Au, Ag, and Cu nanoclusters (<2 nm) on aqueous-phase TiO_2 nanosheets using urea as a basifying and reducing agent. The loading of the metal nanoclusters reached up to 8 wt.%. This high loading is due in part to the fact that TiO_2 is an amphoteric oxide (isoelectric point is 6) [40]. Therefore, TiO_2 surface can adsorb anions in the presence of urea. Under a suitable reaction temperature (90 ˚C), the noble metal anions were reduced by urea into metal nanoclusters on TiO_2 nanosheets with controllable density. As shown in Fig. 1(a), the Au nanoclusters covered the TiO_2 nanosheet surface with controllable loading quantity. The bright-field HRTEM images in Figs. 1(b), 1(d), and 1(f) and dark-field HRTEM images in Figs. 1(c) and 1(e) and Fig. S3(a) in the ESM confirm the uniform loading of Au, Ag, and Cu nanoclusters (<2 nm), respectively, on the TiO_2 nanosheets. By programmable calcination at 300 ˚C, the as-prepared metal nanoclusters could grow into NCs through Ostwald ripening (see also the synthesis scheme in Fig. 2(a)) [41]. As a result, the crystalline contact with the TiO_2 surface is improved, and these materials could act as cocatalysts. The dark- and bright-field TEM images in Fig. 2(b) and Fig. S3(b) in the ESM confirm the uniform Au NCs loading on

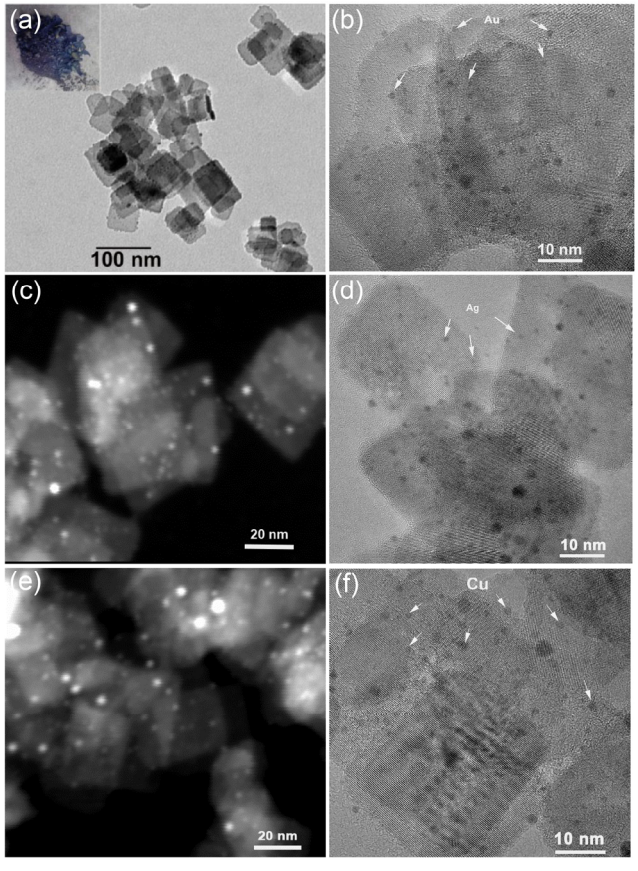

Figure 1 Metal nanoclusters on a TiO_2 nanosheet support: (a) low-resolution TEM image of Au nanoclusters/TiO_2 hybrid nanosheets, the inset shows an image of the gram-scale powder. (b) and (c) Bright- and dark-field HRTEM images, respectively, of Au nanoclusters/TiO_2. (d) and (e) Bright- and dark-field HRTEM images, respectively, of Ag nanoclusters/TiO_2. (f) Bright-field HRTEM image of Cu nanoclusters/TiO_2.

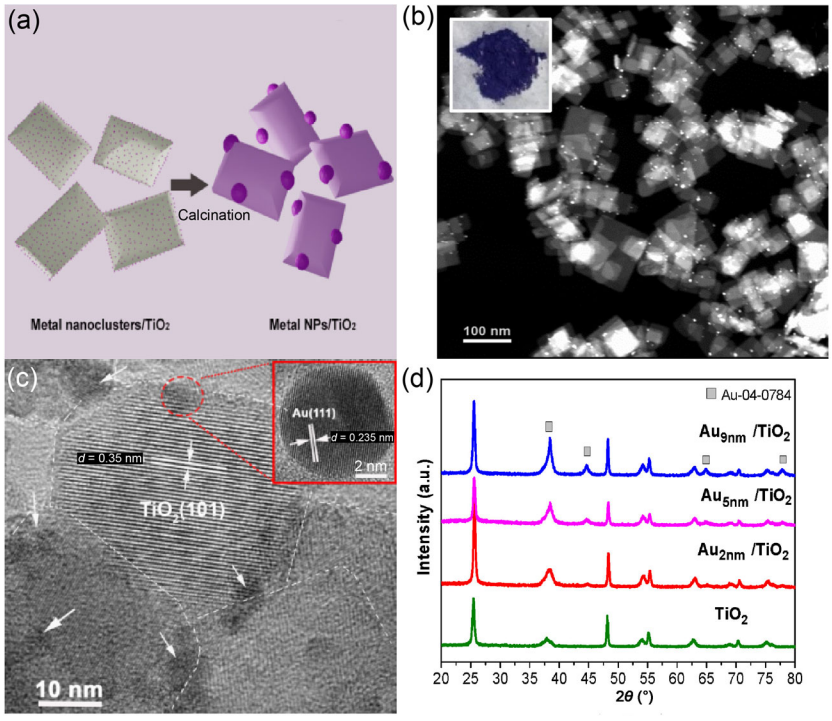

Figure 2 (a) Schematic diagram showing the calcination of metal nanoclusters to form nanocrystals. (b) Dark-field HRTEM image of the cocatalyst Au/TiO_2 hybrid nanostructure after calcination; the inset shows the gram-scale product. (c) HRTEM image of the cocatalyst hybrid Au/TiO_2 showing the close contact and lattice correlations between the Au NCs and anatase TiO_2 nanosheets. (d) XRD patterns of the prepared bare anatase TiO_2 and Au/TiO_2 nanostructures with Au NCs of different sizes.

the TiO_2 nanosheets. Moreover, the ICP-OES results shown in Table S1 (in the ESM) reveal the actual amounts of noble metal loading on the TiO_2 support. The results verify that this aqueous phase synthesis strategy is a facile route to load metal nanoclusters on a TiO_2 support and that subsequent calcination yields metal NCs/TiO_2 hetero-composites (Fig. 2(a)). The average size of the Au NCs was ~9 nm. The color of the gram-scale powder changed from opaque violet before the calcination to luminous blue after the calcination (see inset photographs in Figs. 1(a) and 2(b)), supported the uniform Au NCs/TiO_2 nanosheets hetero-composites formation. The indexed lattice spacings of 0.235 and 0.35 nm, shown in Fig. 2(c), are in good agreement with the interplanar distance of the face-centered cubic (fcc) Au (111) and anatase TiO_2 (101) planes. The HRTEM image indicated good crystalline contact between the Au and TiO_2. By controlling the calcination-induced Ostwald ripening, the Au cocatalyst sizes could be flexibly tuned. Figure 2(d) shows the XRD patterns of the prepared Au/TiO_2 hetero-composites with Au NCs of different sizes. The XRD peaks of anatase TiO_2 (JCPDS no. 21-1272) were observed for all catalyst samples, without any other TiO_2 phases. The other peaks were all related to metallic Au (JCPDS no. 04-0784). The increasingly sharp Au peaks achieved by controlling the Au cocatalyst size verify the good crystallization of the Au cocatalyst after calcination. Furthermore, considering the surface plasmon resonance (SPR) contribution to efficient photocatalysis, this flexible control of the Au size would be beneficial for ensuring that the cocatalyst and plasmon enhancement play synergistic roles.

To demonstrate the versatility of this new strategy, Cu and Ag cocatalysts on TiO_2 nanosheets were also prepared successfully using this calcination-induced Ostwald ripening process [42]. As shown in Fig. 3, the low-resolution TEM images of Cu/TiO_2 (Fig. 3(a)) and Ag/TiO_2 (Fig. 3(c)) verify the uniform Cu and Ag NC loading on the TiO_2 nanosheets with good nanosheet morphology retention. The HRTEM images in Fig. 3(b) (Cu/TiO_2) and Fig. 3(d) (Ag/TiO_2), with well-defined indexed lattice spacings, also confirm the

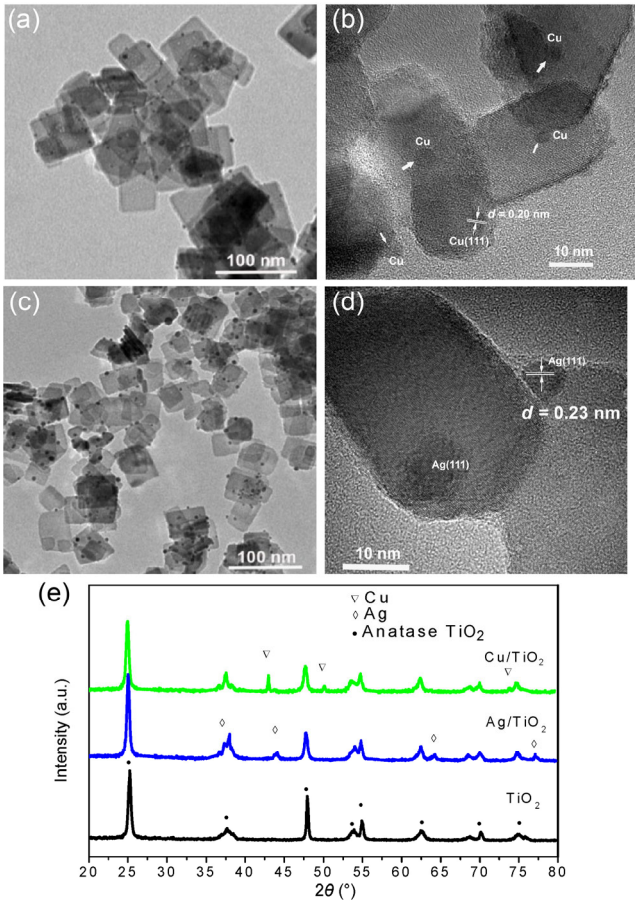

Figure 3 (a) and (b) Low-resolution TEM and HRTEM images, respectively, of the as-synthesized Cu/TiO_2 cocatalyst. (c) and (d) Low-resolution TEM and HRTEM images, respectively, of as-synthesized Ag/TiO_2 cocatalyst. (e) XRD patterns of prepared bare anatase TiO_2, Cu/TiO_2, and Ag/TiO_2 cocatalyst.

good crystallization and strong interface contact with the TiO_2 surface.

The XRD patterns of the as-synthesized hetero-nanosheets compared in Fig. 3(e) clearly show the Cu (JCPDS no. 85-1326) and Ag (JCPDS 87-0717) phase, which is consistent with the HRTEM analysis in Figs. 3(b) and 3(d). The XRD results prove that the loading of metal NCs did not disturb the anatase phase and nanosheet matrix of the TiO_2 photocatalyst. The crystal lattice contact between the anatase TiO_2 and metal NCs is clearly discernable and indicates their excellent junction.

The intimate contact is important for obtaining a true synergetic effect between the cocatalyst and catalyst to enhance the solar energy to hydrogen conversion via efficient photogenerated charge transfer from the semiconductor to metal cocatalysts [43]. The comparison of the UV–Vis absorption spectra in Fig. S5 (in the ESM) demonstrates the enhanced visible light absorption. As the Au NC size increased, the SPR-induced visible light absorption increased as well. When the size of the Au NCs was controlled to be 5–9 nm (see Fig. S6 in the ESM), the SPR peak at 500–550 nm in Fig. S5(a) (in the ESM) became very clear. This increase in the visible light absorption is critical for not only solar light harvesting but also synergistic plasmon-enhanced charge separation [44–47]. As shown in Fig. S5(b) (in the ESM), upon Ag or Cu NC loading, the visible light absorption was also enhanced, although it was not stronger than that of the as-synthesized Au NCs.

Turning our attention to the synthesized M/TiO_2 hybrid nanoclusters, their activities as nanocatalysts in an organic synthesis reaction have been evaluated. Figure 4 shows the synthesized nanoclusters assisted catalytic reduction of 4-nitrophenol into its derivatives, particularly 4-aminophenol. Based on the mass spectrometric analysis, the proposed reaction scheme is depicted in Fig. 4(a). When 4-nitrophenol was reduced in the presence of M/TiO_2 nanoclusters catalyst using this procedure, 4-aminophenol was obtained first, leading to further catalytic reduction, from which the derivative 4-aminophenyl ethyl ether was also obtained. 4-Aminophenol was obtained in 60%, 7%, and 11% yields when using Au/TiO_2, Cu/TiO_2, and Ag/TiO_2 nanocatalyst, respectively (see Fig. 4(b) for comparison). The amount of 4-nitrophenol started to decline rapidly within the first hour, and the amount of product increased rapidly up to 6 h of reaction time, after which the reaction reached equilibrium (see Fig. 4(c)). The effect of the nanocluster catalyst is very clear in Fig. 4(d), in which the reaction yield is 2%–3% without any catalyst and nearly 60% in the presence of the Au/TiO_2 hybrid nanocluster catalyst under the same experimental conditions. Thus, the highly dispersed metal nanoclusters on the support, even with very low loading, demonstrated good heterogeneous catalysis activity.

Motivated by the precise synthesis of M/TiO_2 nanosheets at the gram-scale and their enhanced visible light absorption, their photocatalytic hydrogen production activities have also been studied. Figure 5 shows the hydrogen production under solar light

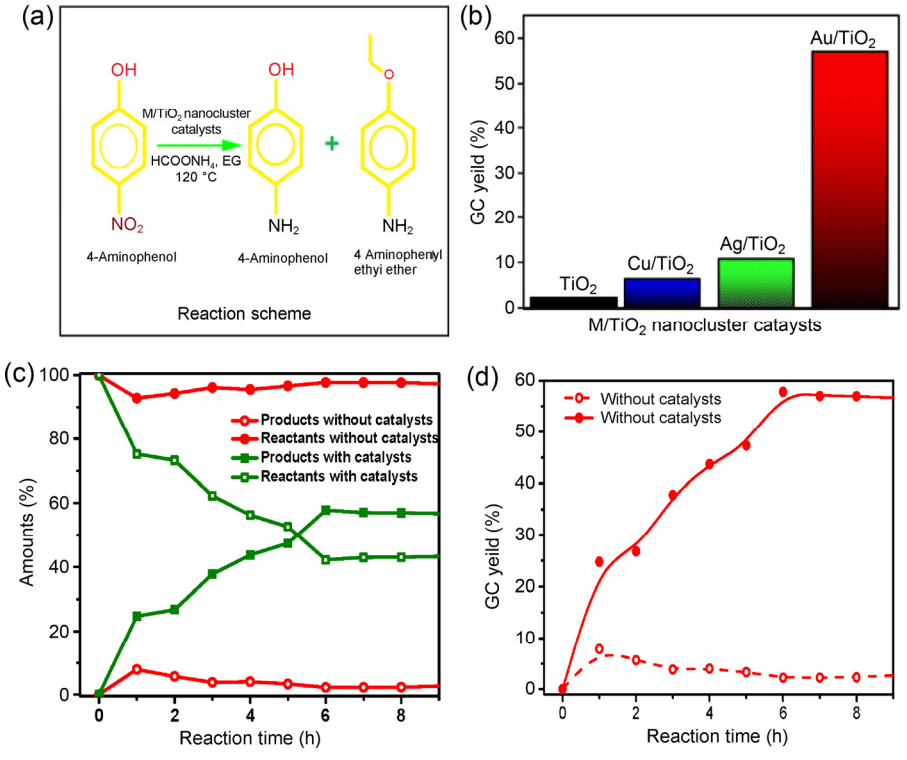

Figure 4 (a) Reaction scheme of 4-nitrophenol reduction assisted by the nanocluster catalyst. (b) Comparison of catalytic reduction GC yields attained using M/TiO_2 nanoclusters. (c) Mass spectrometric analysis of the reaction system. (d) GC yield attained using the Au/TiO_2 nanocluster catalyst.

in the presence of ethanol as a sacrificial agent. As shown in Fig. 5(a), the presence of the Ag, Cu, and Au metal cocatalysts clearly promoted the H_2 evolution rate by several-fold to several-hundred-fold. The maximum activity of the Au_{9nm}/TiO_2 hetero-nanosheets was 2.9 $mmol \cdot g^{-1} \cdot h^{-1}$, which is 320 times higher than that of the bare TiO_2 nanosheets. The calculated quantum efficiency reached 5.18%. The improved photocatalytic activity of M/TiO_2 cocatalysts can be attributed to the SPR enhancement of the electron–hole separation and collection [48]. Under solar light irradiation, the energy band alignment between TiO_2 and noble metal NPs suggests a rapid electron transfer from the conduction band of TiO_2 to the metal NP. In the meantime, the electric field intensified by SPR of the metal constituent can significantly increase the light absorption of the TiO_2 semiconductor and stimulate charge separation near the Au-TiO_2 interface. This synergetic effect increases the amount of electrons (e^-) on the Au surface for efficient water reduction and leads to highly efficient H_2 evolution activity. The poor H_2 evolution activity in the case of small size is mainly attributed to the weak SPR. Calcination increases the stability and activity of the as-synthesized metal/TiO_2 hetero-nanosheets. The catalyst stability and reproducibility play an important role in its performance [49]. Therefore, the photostabilities of the as-synthesized M/TiO_2 catalysts were also investigated. During each 5-h cycle, the photocatalyst was recovered by centrifugation and re-dispersed in deionized water followed by the addition of hole scavengers. After three consecutive cycles, the morphology (Fig. S8 in the ESM) and activity of the used catalyst was well retained, and no appreciable catalyst deactivation was observed, particularly in the case of Au/TiO_2, as shown in Fig. 5(b). However, catalyst aggregation slightly decreased the hydrogen evolution activity of Cu/TiO_2 and Ag/TiO_2, as shown in Fig. S9 (in the ESM). Figure 5(c) compares the H_2 production rates of Au/TiO_2 nanosheets with three different-sized Au NPs and pure TiO_2 nanosheets. The different extents of photoactivity enhancement are due to the different strengths of the SPR effect. The comparatively weak H_2 evolution activity of the Au_{5nm}/TiO_2 is mainly due

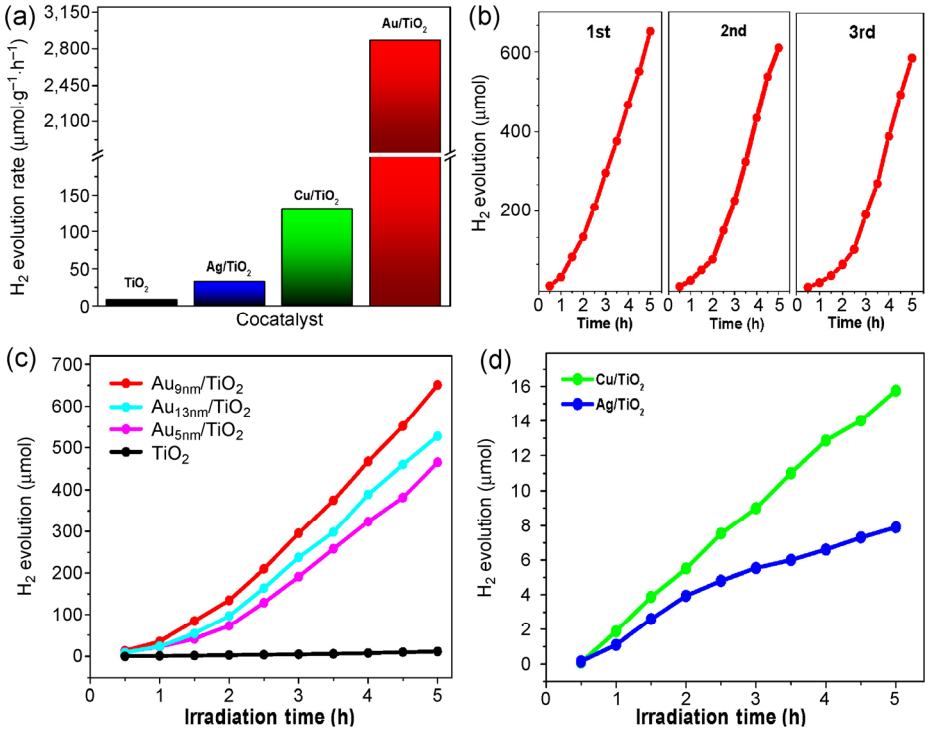

Figure 5 Hydrogen production activities of the as-prepared metal nanocrystal cocatalysts in the presence of ethanol as a sacrificial agent. (a) Comparison of the H_2 evolution activities of the prepared cocatalysts on TiO_2 nanosheets. (b) Recycled H_2 production activities of Au/TiO_2 cocatalyst with ~9 nm Au. (c) Time evolution of photocatalytic generation of H_2 evolution amount versus irradiation time for TiO_2 and Au/TiO_2 nanosheets with different-sized Au NPs. (d) Time evolution of the photocatalytic generation of H_2 evolution amount versus irradiation time for Ag/TiO_2 and Cu/TiO_2 nanosheets.

to the weak SPR and consequent solar light harvesting of smaller Au particles (5 nm) [50–52]. The hydrogen evolution rate increased with the Au particle size up to ~9 nm, but a further increase in the particle size to 13 nm (Fig. S7 in the ESM) decreases the photocatalytic activity, as shown in Fig. 5(c). The decrease in the reaction rate for larger Au is most likely due to a geometric, rather than an electronic, effect. The catalyst with 13-nm Au NPs resulted in an inadequate number of spherical particles, which were simply loaded on the metal oxide support with a lower interface contact area. In contrast, the Au/TiO_2 catalyst with 9-nm Au produced relatively hemispherical NPs in good contact with the TiO_2 support, yielding the largest interface contact area. Additionally, the flexible increase of the Au cocatalyst sizes by calcination will be helpful for constructing an intimate interface and ensuring smooth electron transfer and collection. The photocatalytic H_2 evolution rate of the Cu/TiO_2 and Ag/TiO_2 nanosheets could reach 130 and 32 $\mu mol \cdot h^{-1} \cdot g^{-1}$, respectively, as shown in Figs. 5(a) and 5(d).

To verify the promising and efficient photocatalytic activity of the prepared photocatalysts, we performed photoelectrochemical characterization of their film photoelectrodes. Based on their facile centimeter-scale film deposition on conductive glass (see inset in Fig. 6(a)), the photocurrent responses of bare TiO_2, Au/TiO_2, Cu/TiO_2, and Ag/TiO_2 were examined to study the charge carrier generation. Figures 6(a) and 6(b) demonstrate the photocurrent response of such catalysts under periodic on/off conditions when irradiated with solar light. Figure 6(a) illustrates the photocurrent response of the Au/TiO_2 photocatalyst possessing 9-nm (1) and 5-nm (2) Au NPs. In Fig. 6(b), the bare anatase TiO_2 nanosheets coated on ITO glass exhibit an almost negligible short-circuit photocurrent. However, the loading of metal NPs, especially in the case of Au/TiO_2 nanosheets, markedly increases the photocurrent, and this increment increased linearly with the irradiation time, even with a small amount

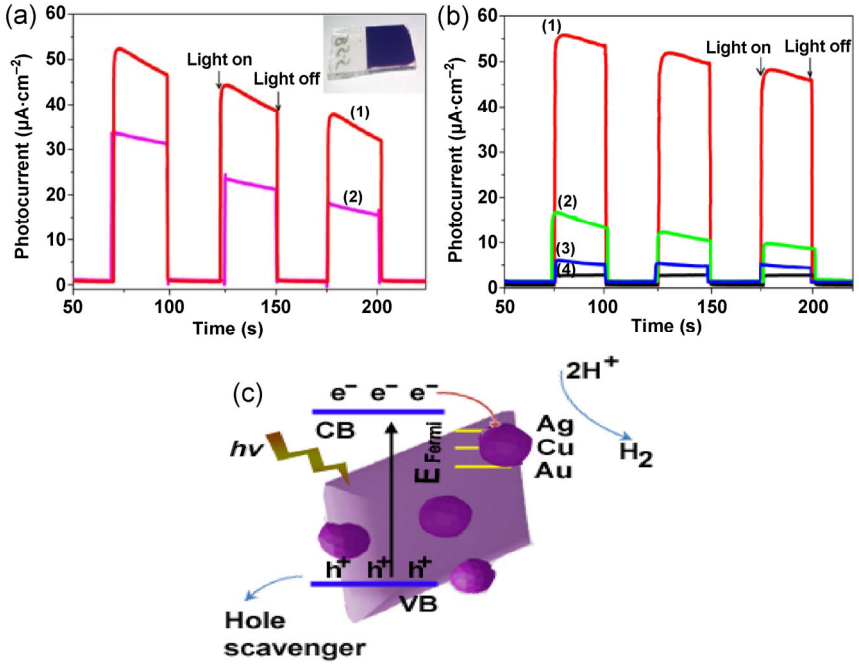

Figure 6 (a) Comparison of the photocurrent response of Au/TiO_2 nanosheet film photoelectrodes with Au NPs of different sizes: (1) 9 nm Au and (2) 5 nm Au. The inset presents a picture of the film-scale photoelectrode. (b) Photocurrent response of (1) Au/TiO_2, (2) Cu/TiO_2, (3) Ag/TiO_2, and (4) bare TiO_2 nanosheets in 0.2 M Na_2SO_4 aqueous electrolyte under solar light irradiation. (c) Schematic diagram of the transfer and separation of photogenerated electrons and holes on the surface of TiO_2.

of Au NP loading. Together with the plasmonic absorption centered at 500–550 nm, this finding indicates that the H_2 evolution is closely related to the localized SPR of Au NPs and can be attributed to the increased light scattering due to the Au NPs [53]. The consistent increasing trend is in strong agreement with the hydrogen evolution rates observed during water-splitting. The photocurrent trends further demonstrate the close correlation between the rate of solar-energy-to-hydrogen conversion and the photocurrent. Here, the enhanced water-splitting photocatalytic activity could be the consequence of the better charge separation and faster electron transfer achieved in M/TiO_2 cocatalysts [54–56], which provides active catalyst sites for hydrogen generation and acts as a as good electron scavenger.

This incredible increase is mostly due to the formation of Schottky barriers along the Au/TiO_2-ITO glass, which accelerates the transfer of photogenerated electrons from TiO_2 to Au and finally to ITO [57]. Moreover, a detailed HRTEM analysis of the M/TiO_2 interface also confirmed that the lattices of Au and TiO_2 are in close contact, and the interfacial portion of the Au NPs is partially buried in a thin layer of TiO_2 nanosheets, indicating that strong contacts have been established between Au and TiO_2 during the calcination process. The close contact between the lattices of the Au and TiO_2 nanocrystals reinforced the Schottky contact. These observations stoutly suggest strong metal–support interactions during the calcination process, which lead to the formation of close Schottky contact at the metal/TiO_2 interface and serve as efficient electron traps, inhibiting electron–hole recombination in photocatalysis [58, 59]. In turn, this often enhances photocatalytic performance. The holes in the photoexcited TiO_2 are quenched by ethanol (the sacrificial electron donor) [60]. The overall H_2 evolution mechanism is presented in Fig. 6(c).

4 Conclusions

In summary, we have successfully prepared M/TiO_2 hybrid nanostructures (M = Cu, Ag, and Au) through a new *in situ* nanoclusters-to-NCs synthesis. The uniformly deposited Cu, Ag, and Au NCs with controllable loading amount, size, and crystallization act

as efficient cocatalysts for active hydrogen evolution and proficient nanoclusters-on-support catalysts for organic catalytic reduction synthesis. The enhanced H_2 production activity and more sensitive photoresponse of the as-synthesized photocatalysts confirm that the metal cocatalysts increase the hydrogen evolution efficiency. Specifically, the intimate contact between the metal NCs and TiO_2 nanosheets provides fast electron generation and transport by inhibiting electron–hole pair recombination. A promising quantum efficiency of 5.18% could be achieved using the Au/TiO_2 photocatalyst. In addition to the efficient cocatalyst preparation, the uniform loading of noble metal nanoclusters on transitional metal oxide catalysts attained using our strategy provides a potential alternative to new built-up metal nanocluster catalysts.

Acknowledgements

This work was supported by the National Natural Science Foundation of China (Nos. 21322105, 51372025 and 913233001), the Research Fund for the Doctoral Program of Higher Education of China (No. 2011101120016), and Program for New Century Excellent Talents in University (No. NCET-11-0793).

Electronic Supplementary Material: Supplementary material (TEM, HRTEM and SEM images of as prepared anatase TiO_2 nanosheets, TEM, dark-field TEM images, UV–Vis absorption spectra, photograph images showing color evolution during synthesis of M/TiO_2 hybrid nanostructures, ICP-OES results, TEM image of used catayst, cycling tests and detailed calculation of quantum efficiency) is available in the online version of this article at http://dx.doi.org/10.1007/s12274-016-1069-y.

References

[1] Valden, M.; Lai, X.; Goodman, D. W. Onset of catalytic activity of gold clusters on titania with the appearance of nonmetallic properties. *Science* **1998**, *281*, 1647–1650.

[2] Häkkinen, H.; Moseler, M.; Landman, U. Bonding in Cu, Ag, and Au clusters: Relativistic effects, trends, and surprises. *Phys. Rev. Lett.* **2002**, *89*, 033401.

[3] Chen, S. F.; Li, J. P.; Qian, K.; Xu, W. P.; Lu, Y.; Huang, W. X.; Yu, S. H. Large scale photochemical synthesis of M@TiO_2 nanocomposites (M = Ag, Pd, Au, Pt) and their optical properties, CO oxidation performance, and antibacterial effect. *Nano Res.* **2010**, *3*, 244–255.

[4] DuChene, J. S.; Sweeny, B. C.; Johnston-Peck, A. C.; Su, D.; Stach, E. A.; Wei, W. D. Prolonged hot electron dynamics in plasmonic-metal/semiconductor heterostructures with implications for solar photocatalysis. *Angew. Chem., Int. Ed.* **2014**, *53*, 7887–7891.

[5] Chen, M. S.; Goodman, D. W. Catalytically active gold: From nanoparticles to ultrathin films. *Acc. Chem. Res.* **2006**, *39*, 739–746.

[6] Bell, A. T. The impact of nanoscience on heterogeneous catalysis. *Science* **2003**, *299*, 1688–1691.

[7] Du, M. M.; Sun, D. H.; Yang, H. W.; Huang, J. L.; Jing, X. L.; Odoom-Wubah, T.; Wang, H. T.; Jia, L. S.; Li, Q. B. Influence of Au particle size on Au/TiO_2 catalysts for CO oxidation. *J. Phys. Chem. C* **2014**, *118*, 19150–19157.

[8] Corma, A.; Garcia, H. Supported gold nanoparticles as catalysts for organic reactions. *Chem. Soc. Rev.* **2008**, *37*, 2096–2126.

[9] Li, G.; Jin, R. C. Atomically precise gold nanoclusters as new model catalysts. *Acc. Chem. Res.* **2013**, *46*, 1749–1758.

[10] Claus, P.; Brückner, A.; Mohr, C.; Hofmeister, H. Supported gold nanoparticles from quantum dot to mesoscopic size scale: Effect of electronic and structural properties on catalytic hydrogenation of conjugated functional groups. *J. Am. Chem. Soc.* **2000**, *122*, 11430–11439.

[11] Qi, D. Y.; Yan, X. F.; Wang, L. Z.; Zhang, J. L. Plasmon-free SERS self-monitoring of catalysis reaction on Au nanoclusters/TiO_2 photonic microarray. *Chem. Commun.* **2015**, *51*, 8813–8816.

[12] Lin, Z. J.; Wang, X. H.; Liu, J.; Tian, Z. Y.; Dai, L. C.; He, B. B.; Han, C.; Wu, Y. Q.; Zeng, Z. G.; Hu, Z. Y. On the role of localized surface plasmon resonance in UV-Vis light irradiated Au/TiO_2 photocatalysis systems: Pros and cons. *Nanoscale* **2015**, *7*, 4114–4123.

[13] Zhang, X.; Liu, Y.; Lee, S. T.; Yang, S. H.; Kang, Z. H. Coupling surface plasmon resonance of gold nanoparticles with slow-photon-effect of TiO_2 photonic crystals for synergistically enhanced photoelectrochemical water splitting. *Energy Environ. Sci.* **2014**, **7**, 1409–1419.

[14] Yang, J. H.; Wang, D.; Han, H. X.; Li, C. Roles of cocatalysts in photocatalysis and photoelectrocatalysis. *Acc. Chem. Res.* **2013**, *46*, 1900–1909.

[15] Shen, J. F.; Shi, M.; Yan, B.; Ma, H. W.; Li, N.; Ye, M. X. Ionic liquid-assisted one-step hydrothermal synthesis of TiO_2-reduced graphene oxide composites. *Nano Res.* **2011**, *4*, 795–806.

[16] Turner, J. A. Sustainable hydrogen production. *Science* **2004**, *305*, 972–974.

[17] Liu, Y. C.; Gu, Y. S.; Yan, X. Q.; Kang, Z.; Lu, S. N.; Sun, Y. H.; Zhang, Y. Design of sandwich-structured ZnO/ZnS/Au photoanode for enhanced efficiency of photoelectrochemical water splitting. *Nano Res.* **2015**, *8*, 2891–2900.

[18] Cortright, R. D.; Davda, R. R.; Dumesic, J. A. Hydrogen from catalytic reforming of biomass-derived hydrocarbons in liquid water. *Nature* **2002**, *418*, 964–967.

[19] Sajan, C. P.; Wageh, S.; Al-Ghamdi, A. A.; Yu, J. G.; Cao, S. W. TiO_2 nanosheets with exposed {001} facets for photocatalytic applications. *Nano Res.* **2016**, *9*, 3–27.

[20] Fujishima, A.; Honda, K. Electrochemical photolysis of water at a semiconductor electrode. *Nature* **1972**, *238*, 37–38.

[21] Han, X. G.; Kuang, Q.; Jin, M. S.; Xie, Z. X.; Zheng, L. S. Synthesis of titania nanosheets with a high percentage of exposed (001) facets and related photocatalytic properties. *J. Am. Chem. Soc*. **2009**, *131*, 3152–3153.

[22] Yang, H. G.; Sun, C. H.; Qiao, S. Z.; Zou, J.; Liu, G.; Smith, S. C.; Cheng, H. M.; Lu, G. Q. Anatase TiO_2 single crystals with a large percentage of reactive facets. *Nature* **2008**, *453*, 638–641.

[23] Xing, M.-Y.; Yang, B.-X.; Yu, H.; Tian, B.-Z.; Bagwasi, S.; Zhang, J.-L.; Gong, X.-Q. Enhanced photocatalysis by Au nanoparticle loading on TiO_2 single-crystal (001) and (110) facets. *J. Phys. Chem. Lett.* **2013**, *4*, 3910–3917.

[24] Chen, X. B.; Mao, S. S. Titanium dioxide nanomaterials: Synthesis, properties, modifications and applications. *Chem. Rev*. **2007**, *107*, 2891–2959.

[25] Ni, M.; Leung, M. K. H.; Leung, D. Y. C.; Sumathy, K. A review and recent developments in photocatalytic water-splitting using TiO_2 for hydrogen production. *Renew. Sustain. Energ. Rev*. **2007**, *11*, 401–425.

[26] Osterloh, F. E. Inorganic materials as catalysts for photochemical splitting of water. *Chem. Mater*. **2008**, *20*, 35–54.

[27] Ismail, A. A.; Bahnemann, D. W. Photochemical splitting of water for hydrogen production by photocatalysis: A review. *Sol. Energy Mater. Sol. Cells* **2014**, *128*, 85–101.

[28] Zhang, Z. Y.; Wang, Z.; Cao, S.-W.; Xue, C. Au/Pt nanoparticle-decorated TiO_2 nanofibers with plasmon-enhanced photocatalytic activities for solar-to-fuel conversion. *J. Phys. Chem. C* **2013**, *117*, 25939–25947.

[29] Subramanian, V.; Wolf, E.; Kamat, P. V. Semiconductor-metal composite nanostructures. To what extent do metal nanoparticles improve the photocatalytic activity of TiO_2 films? *J. Phys. Chem. B* **2001**, *105*, 11439–11446.

[30] Pearson, A.; Zheng, H. D.; Kalantar-Zadeh, K.; Bhargava, S. K.; Bansal, V. Decoration of TiO_2 nanotubes with metal nanoparticles using polyoxometalate as a UV-switchable reducing agent for enhanced visible and solar light photocatalysis. *Langmuir* **2012**, *28*, 14470–14475.

[31] Yu, X. L.; Shavel, A.; An, X. Q.; Luo, Z. S.; Ibáñez, M.; Cabot, A. Cu_2ZnSnS_4-Pt and Cu_2ZnSnS_4-Au heterostructured nanoparticles for photocatalytic water splitting and pollutant degradation. *J. Am. Chem. Soc.* **2014**, *136*, 9236–9239.

[32] Kochuveedu, S. T.; Jang, Y. H.; Kim, D. H. A study on the mechanism for the interaction of light with noble metal-metal oxide semiconductor nanostructures for various photophysical applications. *Chem. Soc. Rev.* **2013**, *42*, 8467–8493.

[33] Long, R.; Prezhdo, O. V. Instantaneous generation of charge-separated state on TiO_2 surface sensitized with plasmonic nanoparticles. *J. Am. Chem. Soc*. **2014**, *136*, 4343–4354.

[34] Chen, Y. S.; Choi, H.; Kamat, P. V. Metal-cluster-sensitized solar cells. A new class of thiolated gold sensitizers delivering efficiency greater than 2%. *J. Am. Chem. Soc.* **2013**, *135*, 8822–8825.

[35] Xiao, F. X. Layer-by-layer self-assembly construction of highly ordered metal-TiO_2 nanotube arrays heterostructures (M/TNTs, M = Au, Ag, Pt) with tunable catalytic activities. *J. Phys. Chem. C* **2012**, *116*, 16487–16498.

[36] Delannoy, L.; Thrimurthulu, G.; Reddy, P. S.; Méthivier, C.; Nelayah, J.; Reddy, B. M.; Ricolleau, C.; Louis, C. Selective hydrogenation of butadiene over TiO_2 supported copper, gold and gold-copper catalysts prepared by deposition-precipitation. *Phys. Chem. Chem. Phys*. **2014**, *16*, 26514–26527.

[37] Kisch, H.; Bahnemann, D. Best practice in photocatalysis: Comparing rates or apparent quantum yields? *J. Phys. Chem. Lett*. **2015**, *6*, 1907−1910.

[38] Zhang, J. Y.; Wang, Y. H.; Jin, J.; Zhang, J.; Lin, Z.; Huang, F.; Yu, J. G. Efficient visible-light photocatalytic hydrogen evolution and enhanced photostability of core/shell CdS/g-C_3N_4 nanowires. *ACS Appl. Mater. Interfaces* **2013**, *5*, 10317−10324.

[39] Li, Q.; Guo, B. D.; Yu, J. G.; Ran, J. R.; Zhang, B. H.; Yan, H. J.; Gong, J. R. Highly efficient visible-light-driven photocatalytic hydrogen production of CdS-cluster-decorated graphene nanosheets. *J. Am. Chem. Soc*. **2011**, *133*, 10878–10884.

[40] Boehm, H. P. Functional groups on the surfaces of solids. *Angew. Chem., Int. Ed.* **1966**, *5*, 533–544.

[41] Sun, Y. G. Controlled synthesis of colloidal silver nanoparticles in organic solutions: Empirical rules for nucleation engineering. *Chem. Soc. Rev*. **2013**, *42*, 2497–2511.

[42] Liu, Y. Z.; Sun, Y. G. Electron beam induced evolution in Au, Ag, and interfaced heterogeneous Au/Ag nanoparticles. *Nanoscale* **2015**, *7*, 13687–13693.

[43] Ding, D. W.; Liu, K.; He, S. N.; Gao, C. B.; Yin, Y. D. Ligand-exchange assisted formation of Au/TiO_2 schottky contact for visible-light photocatalysis. *Nano Lett*. **2014**, *14*, 6731–6736.

[44] Zhao, Q.; Ji, M. W.; Qian, H. M.; Dai, B. S.; Weng, L.; Gui, J.; Zhang, J. T.; Ouyang, M.; Zhu, H. S. Controlling structural symmetry of a hybrid nanostructure and its effect on efficient photocatalytic hydrogen evolution. *Adv. Mater.* **2014**, *26*, 1387–1392.

[45] Bai, S.; Jiang, J.; Zhang, Q.; Xiong, Y. J. Steering charge kinetics in photocatalysis: Intersection of materials syntheses, characterization techniques and theoretical simulations. *Chem. Soc. Rev*. **2015**, *44*, 2893–2939.

[46] Zheng, D. J.; Pang, X. C.; Wang, M. Y.; He, Y. J.; Lin, C. J.; Lin, Z. Q. Unconventional route to hairy plasmonic/semiconductor core/shell nanoparticles with precisely controlled dimensions and their use in solar energy conversion. *Chem. Mater*. **2015**, *27*, 5271–5278.

[47] Linic, S.; Christopher, P.; Ingram, D. B. Plasmonic-metal nanostructures for efficient conversion of solar to chemical energy. *Nat. Mater*. **2011**, *10*, 911–921.

[48] Pu, Y. C.; Wang, G. M.; Chang, K. D.; Ling, Y. C.; Lin, Y. K.; Fitzmorris, B. C.; Liu, C. M.; Lu, X. H.; Tong, Y. X.; Zhang, J. Z. et al. Au nanostructure-decorated TiO_2 nanowires exhibiting photoactivity across entire UV-visible region for photoelectrochemical water splitting. *Nano Lett.* **2013**, *13*, 3817–3823.

[49] Buriak, J. M.; Kamat, P. V.; Schanze, K. S. Best practices for reporting on heterogeneous photocatalysis. *ACS Appl. Mater. Interfaces* **2014**, *6*, 11815−11816.

[50] Subramanian, V.; Wolf, E. E.; Kamat, P. V. Catalysis with TiO_2/gold nanocomposites. Effect of metal particle size on the Fermi level equilibration. *J. Am. Chem. Soc*. **2004**, *126*, 4943–4950.

[51] Dang, X. N.; Qi, J. F.; Klug, M. T.; Chen, P. Y.; Yun, D. S.; Fang, N. X.; Hammond, P. T.; Belcher, A. M. Tunable localized surface plasmon-enabled broadband light-harvesting enhancement for high-efficiency panchromatic dye-sensitized solar cells. *Nano Lett*. **2013**, *13*, 637–642.

[52] Seh, Z. W.; Liu, S. H.; Low, M.; Zhang, S. Y.; Liu, Z. L.; Mlayah, A.; Han, M. Y. Janus Au-TiO_2 photocatalysts with strong localization of plasmonic near-fields for efficient visible-light hydrogen generation. *Adv. Mater*. **2012**, *24*, 2310–2314.

[53] Liu, L. P.; Wang, G. M.; Li, Y.; Li, Y. D.; Zhang, J. Z. CdSe quantum dot-sensitized Au/TiO_2 hybrid mesoporous films and their enhanced photoelectrochemical performance. *Nano Res.* **2011**, *4*, 249–258.

[54] Chen, G.; Zhao, Y.; Shang, L.; Waterhouse, G. I. N.; Kang, X.; Wu, L. Z.; Tung, C. H.; Zhang, T. R. Recent advances in the synthesis, characterization and application of Zn^+-containing heterogeneous catalysts. *Adv. Sci.* **2016**, 1500424.

[55] Lu, Q. P.; Lu, Z. D.; Lu, Y. Z.; Lv, L. F.; Ning, Y.; Yu, H. X.; Hou, Y. B.; Yin, Y. D. Photocatalytic synthesis and photovoltaic application of Ag-TiO_2 nanorod composites. *Nano Lett*. **2013**, *13*, 5698–5702.

[56] Bian, Z. F.; Tachikawa, T.; Zhang, P.; Fujitsuka, M.; Majima, T. Au/TiO_2 superstructure-based plasmonic photocatalysts exhibiting efficient charge separation and unprecedented activity. *J. Am. Chem. Soc*. **2014,** *136*, 458–465.

[57] Chen, H. J.; Liu, G.; Wang, L. Z. Switched photocurrent direction in Au/TiO_2 bilayer thin films. *Sci. Rep*. **2015**, *5*, 10852.

[58] Lee, J.; Mubeen, S.; Ji, X. L.; Stucky, G. D.; Moskovits, M. Plasmonic photoanodes for solar water splitting with visible light. *Nano Lett*. **2012**, *12*, 5014–5019.

[59] Kamat, P. V. Manipulation of charge transfer across semiconductor interface. A criterion that cannot be ignored in photocatalyst design. *J. Phys. Chem. Lett*. **2012**, *3*, 663–672.

[60] Waterhouse, G. I. N.; Wahab, A. K.; Al-Oufi, M.; Jovic, V.; Anjum, D. H.; Sun-Waterhouse, D.; Llorca, J.; Idriss, H. Hydrogen production by tuning the photonic band gap with the electronic band gap of TiO_2. *Sci. Rep*. **2013**, *3*, 2849.